nature communications

Article

https://doi.org/10.1038/s41467-025-61510-w

Dislocation-assisted electron and hole transport in GaN epitaxial layers

Received: 1 November 2024

Accepted: 24 June 2025

Published online: 12 July 2025

Check for updates

Yixu Yao[1], Sen Huang[1] ✉, Ruyue Cao[2,3], Zhaofu Zhang[4], Xinhua Wang[1], Qimeng Jiang[1], Jingyuan Shi[1], Chenrui Zhang[1], Jiaolong Liu[1], Ke Wei[1], Yi Pei[5], Hui Zhang[5], Hongtu Qian[5], Fuqiang Guo[6], Guoping Li[6], Ning Tang[6], Jun-Wei Luo[3], Weikun Ge[6], Xinyu Liu[1] ✉, Bo Shen[6] ✉ & Kevin J. Chen[7] ✉

Dislocations significantly influence carrier transport in semiconductors. While segments orthogonal to the channel act as scattering centers impeding conduction, electrically active dislocation cores can facilitate carrier transport. However, the mechanisms governing carrier transport along dislocation cores remain unclear. Here, we provide the first experimental evidence for the separate transport mechanisms of electrons and holes mediated by threading screw dislocations and threading edge dislocations in gallium nitride. Critically, we demonstrate that devices with a higher total dislocation density exhibit less degradation due to current collapse, owing to a larger proportion of edge dislocations mitigating electron trapping caused by screw dislocations. Screw dislocations promote electron leakage via horizontal potential barriers and vertically connected shallow states, while edge dislocations enhance hole transport through extended trap levels interacting with buffer defects. These findings clarify the long-standing debate on carrier-specific dislocation transport mechanisms and offer critical insights for defect engineering, epitaxial growth optimization, and the development of dislocation-enhanced semiconductor devices.

Dislocations, as ubiquitous line defects in crystal structures, have long been pivotal in materials science due to their profound influence on material properties. Over the past decades, precise experimental and theoretical advancements have significantly deepened our understanding of dislocation formation[1,2], structures[3], phonon interactions[4], and even atom diffusion along the dislocation[5]. This knowledge has facilitated improved defect management strategies in electronic device design. It is well-established that dislocation segments orthogonal to the channel direction act as scattering centers[6], impeding carrier transport, whereas electrically active cores along threading dislocations facilitate carrier conduction. However, the complexity of dislocation-mediated conduction means that many critical aspects remain poorly understood. These include interactions between dislocations and point defects, the formation of quantum wells along dislocation lines, and the precise mechanisms governing charge carrier transport along dislocations[7–9]. Investigating dislocations as carrier transport channels is essential, as their presence significantly influences electronic device performance, manifesting in effects such as breakdown, leakage currents, and dynamic degradation. Moreover, understanding carrier transport along dislocations can provide a foundation for the development of dislocation-based electronic devices and opens new avenues for defect engineering[10].

[1]Institute of Microelectronics, Chinese Academy of Sciences, Beijing 100029, China. [2]Department of Engineering, University of Cambridge, Cambridge CB2 1PZ, UK. [3]Institute of Semiconductors, Chinese Academy of Sciences, Beijing 100083, China. [4]Institute of Technological Sciences, Wuhan University, Wuhan, Hubei 430072, China. [5]Dynax Semiconductor, Suzhou, Jiangsu 215300, China. [6]School of Physics, Peking University, Beijing 100871, China. [7]Department of Electronic and Computer Engineering, Hong Kong University of Science and Technology, Clear Water Bay, Kowloon 999077, Hong Kong.
✉e-mail: huangsen@ime.ac.cn; xyliu@ime.ac.cn; bshen@pku.edu.cn; eekjchen@ust.hk

An ongoing debate in dislocation conductivity is whether individual dislocations transport both electrons and holes, or if different types of dislocations are responsible for the separate transport of these charge carriers[11–14]. In silicon, studies have suggested that dislocations can facilitate the transport of both electrons and holes. This conclusion is based on observations where both p-MOSFETs and n-MOSFETs exhibited higher current levels in samples with high concentrations of horizontal dislocations[7]. However, an increase of the drain current of n-MOSFETs with decreasing number of dislocations was also stated in some research[11,15,16]. These studies did not distinguish between different types of dislocations, leaving the debate unresolved. Research on diamond has shown that two types of dislocations possess capture cross-sections for electrons and holes that differ by several orders of magnitude[17], indicating that electrons and holes are likely transported by different types of dislocations. In perovskites, studies have revealed that oxygen vacancies migrate from the bulk crystal to dislocation cores, resulting in the formation of negative space-charge tubes[18]. However, this studies primarily focus on the aggregation of elements, rather than exploring the charge transport channels inherently associated with the dislocations themselves. Furthermore, the precise mechanism of carrier transport through dislocations remains unclear. There is no definitive evidence to determine whether carriers are transported via nearest-neighbor one-dimensional hopping[19] introduced by dislocations or through vertically extended localized states[20], akin to a one-dimensional electron gas (1-DEG) or hole gas (1-DHG)[21]. Existing studies have thus far been limited to theoretical proposals, leaving the exact transport mechanism unresolved.

Clarifying this distinction is key to developing precise defect management strategies, especially in wurtzite gallium nitride (GaN). GaN epitaxial layers often exhibit high dislocation densities (10^6 to 10^{10} cm^{-2}) due to lattice and thermal mismatches during heteroepitaxial growth on substrates like sapphire[22–24]. In GaN-based optoelectronic devices operating at 365 nm wavelengths, dislocations induce radiative/non-radiative recombination through defect-associated energy levels, significantly degrading blue luminous efficiency. This fundamental limitation drives intensive efforts to minimize dislocation densities in photonic applications. However, dislocation management strategies in electronic devices may require nuanced consideration, particularly given the above-mentioned unresolved carrier transport characteristics across different dislocation types in GaN. The functional dichotomy of defects becomes evident when comparing semiconductor engineering paradigms. In silicon IGBTs, controlled minority carrier injection enhances device performance through two mechanisms: (1) accelerated switching via carrier recombination, and (2) improved breakdown voltage through charge compensation effects. Similarly, GaN power devices employ carbon doping to achieve comparable breakdown enhancement via deep-level compensation. This context underscores the critical need for dislocation characterization to enable targeted device optimization.

The ambivalent role of dislocations manifests distinctly in GaN HEMT operation. Electron transport through threading dislocations introduces three detrimental effects: (1) increased leakage currents through conductive dislocation cores, (2) parasitic depletion of two-dimensional electron gas (2DEG) carriers, and (3) enhanced electron scattering leading to elevated channel resistance[25–27]. Conversely, vertical hole transport along dislocations in GaN buffer layers demonstrates beneficial impacts on dynamic on-resistance (R_{ON}) characteristics by facilitating hole injection and recombination dynamics[28–30]. This transport asymmetry highlights the necessity for dislocation-type-specific engineering approaches in GaN electronics.

The dislocations within the hexagonal system of GaN also exhibit intricate electronic structures and transport properties that existing theories for cubic crystals fail to explain. Three types of threading dislocations are present in GaN: threading screw dislocations (TSDs), threading edge dislocations (TEDs), and threading mixed dislocations. Threading mixed dislocations, resulting from the superposition of screw and edge components, have diverse and variable atomic structures. Consequently, research on mixed dislocations is typically pursued after a thorough investigation of the more fundamental TSDs and TEDs. Furthermore, in the epitaxial structure of AlGaN/GaN power devices, a carbon-doped GaN buffer layer is widely adopted to raise the energy band barrier between the active layer and the substrate, thereby confining the downward penetration of electrons, thereby enhancing the breakdown voltage of the device. There is strong evidence that the interaction between dislocations and the carbon-doped buffer layer plays a decisive role in the dynamic on-resistance (R_{ON}) and breakdown of GaN-based power devices[14,28,29].

The TSDs in GaN are characterized by a Burgers vector parallel to the dislocation line, with atomic planes spiraling around the dislocation core, resembling a staircase where each step is an additional atomic plane. These dislocations are associated with shear stresses and exhibit simpler elastic distortions. Studies have shown that TSDs act as conduction pathways for charge carriers, making them a major source of leakage currents and breakdown in GaN devices[31–36]. Various TSD core structures—full-core, filled-core, and open-core—have been theoretically studied[37], with the open-core screw dislocation (7.2 Å diameter) showing the lowest formation energy under typical nitrogen-rich metal-organic chemical vapor deposition (MOCVD) GaN growth conditions[3,38–40]. However, the mechanisms of carrier transport through these dislocations are not yet well understood.

On the other hand, TEDs in GaN have a Burgers vector perpendicular to the dislocation line and lie in the plane, involving an extra half-plane of atoms within the crystal lattice. This configuration introduces both tensile and compressive stresses, leading to more complex elastic distortions. Depending on their core structure, TEDs can introduce shallow or deep energy levels, indirectly impacting device performance in high-voltage and high-frequency switching operations[41]. The gallium-vacancy type TEDs, the most favorable core configuration in the nitrogen-rich growth environment of MOCVD-grown GaN, has the lowest formation energy[42–44]. Despite theoretical predictions, experimental evidence for the behavior of gallium-vacancy TEDs remains scarce, leaving their mechanisms in GaN unclear.

In this study, we aim to bridge this knowledge gap by elucidating the distinct roles of TSDs and TEDs in electron and hole transport within the GaN. By employing a comprehensive approach involving cryogenic photoluminescence spectroscopy, conductive atomic force microscopy, electrostatic force microscopy, deep-level transient spectroscopy, and isothermal capacitance transient techniques, we provide the first experimental evidence for the separate transport mechanisms of electrons and holes mediated by TSDs and TEDs in GaN. Our findings reveal that:

(a) The open-core type screw dislocation creates horizontal electron potential wells and vertically aligned shallow electronic states due to gallium dangling bonds and Ga–N dipoles along the dislocation sidewall. This configuration induces electron leakage and current collapse at elevated voltages, making TSDs a critical factor in device reliability.

(b) The gallium-vacancy type edge dislocations introduce an extended hole trap positioned above the valence band maximum, facilitating the transport of holes ionized from C_N defects within the carbon-doped GaN buffer. This mechanism aids in alleviating the degradation of dynamic R_{ON}, enhancing device performance during high-voltage and high-frequency operations.

We demonstrate that devices with a higher total dislocation density exhibit smaller current collapse degradation due to the larger proportion of TEDs mitigating electron trapping caused by TSDs. Understanding this dual-path transport mechanism not only clarifies the long-standing debate on the roles of different dislocations in carrier transport but also provides crucial insights for optimizing epitaxial

https://doi.org/10.1038/s41467-025-61510-w

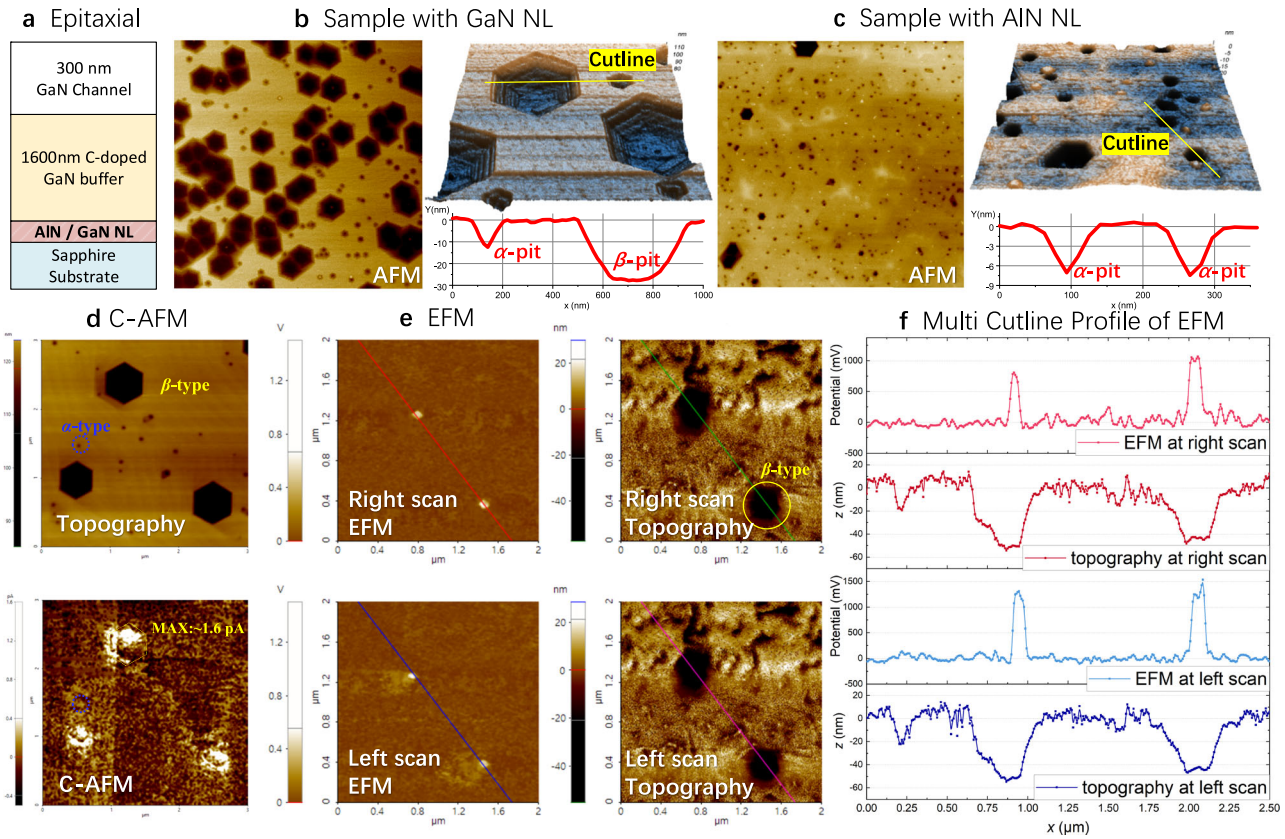

Fig. 1 | Dislocation-type characterization in GaN epitaxy. a Different epitaxial sequences and AFM images of samples: (**b**) with GaN and (**c**) with AlN nucleation layer. The large trapezoidal β-type pits are associated with screw dislocations (TSDs), while the small triangular α-type pits are originated from edge dislocations (TEDs). The samples are referred to as TSD-dominant and TED-dominant, respectively. **d** Dislocation induced leakage current in GaN: Topography and c-AFM images, the yellow dotted line outlines the edge of the β-pit; The leakage generated by TED *α*-type pits (blue circle marked) in c-AFM is below the noise level of 0.4 pA, while the leakage current distribution corresponding to open-core TSD at six surfaces of *β*-type etching pits is uneven, and the maximum of leakage is about 1.6 pA. **e** Electric potential distribution of TSDs in GaN: Topography and EFM with left and right scan images and (**f**) multi cutline profile of EFM; The EFM corresponding to the β-type pit is a light spot, with a potential well about 1 V higher than the surface potential.

growth, laying the foundation for further utilization of dislocations in designing dislocation-enhanced devices and potentially pioneering dislocation-based devices.

Results

Fabrication of TSD- and TED-dominant GaN Epitaxy

To introduce distinct dislocation configurations, two GaN epitaxial structures were grown on sapphire substrates via metal-organic chemical vapor deposition (MOCVD). For TSD-dominant samples, a tailored two-step GaN nucleation layer (NL) was employed: (1) a low-temperature (LT) GaN layer to nucleate small grains, followed by (2) a high temperature, low pressure, and high V(NH_3)/III(TEG) ratio 3D-GaN layer (a) to promote screw dislocation formation. This process leverages compressive stress from 3D island coalescence to suppress tilt components (edge dislocations) while retaining twist components (screw dislocations). In contrast, TED-dominant samples utilized a conventional AlN NL, which facilitates tensile stress relaxation via edge dislocation proliferation. Both samples subsequently underwent identical carbon-doped GaN buffer and channel layer growth. The differences in growth conditions and epitaxial stress information are shown in Supplementary Information Figs. S1 and S2. The TEM, SEM, and XRD results for verifying the prevalence of threading screw dislocations and edge dislocations are shown in Supplementary Information Figs. S3, S4, and S5 and Table. S1, respectively. Other growth conditions for GaN epitaxy, including the carbon-doping level in the GaN buffer, were kept identical for both samples. The epitaxial structure of the sample is shown in Fig. 1a. The distinction in dislocation density and types between the two samples was determined after subjecting them to a molten KOH etching process for 6 minutes in a nickel crucible at 400 °C.

Figure 1b, c illustrates the surface morphology scanned by AFM of both samples after molten KOH etching. The cutline profile shows two kinds of dislocation-related etching pits on the surface, named α- and β-type pits. The inverted trapezoid β-type pit is identified to be the open-core screw dislocation[45], and the small sharp triangular α-type pit originates from the threading edge dislocations[46]. It can be observed that the density of the open-core TSDs in the sample with the GaN NL is significantly higher than that in the sample with AlN NL, whereas a higher TED density was observed in the sample with AlN NL (the actual density of TED of the sample with GaN NL might be higher because of the α-type pit merging into the larger β-type pits). To facilitate comprehension, we refer to the samples with the AlN and GaN NL as the "TED dominant" sample and "TSD-dominant" sample, respectively. Table 1 estimates the number of two type dislocations, note that the total number of dislocations in the TED dominant sample is about 2 times higher than that in the TSD dominant sample.

EFM and c-AFM Characterization of TSD- and TED-dominant Epitaxy

To confirm the basic characteristics of these dislocations in situ, semi-quantitative electrostatic force microscopy (EFM) and c-AFM modes based on AFM were adopted to confirm the potential changes

Table 1 | Comparison of Threading Dislocation Types and Densities (Estimated by Etching Pits)

Sample	TSDs	TSD-induced electron traps	TEDs	TED-induced hole traps
With GaN NL (TSD-dominant)	~4.2×10^{8} cm^{-2}	~5×10^{16} cm^{-3}	~3.8×10^{8} cm^{-2}	0.72×10^{16} cm^{-3}
With AlN NL (TED-dominant)	~0.2×10^{8} cm^{-2}	~0.2×10^{16} cm^{-3}	~18×10^{8} cm^{-2}	3.4×10^{16} cm^{-3}

corresponding to these dislocation pits and the possible leakage channels introduced. The c-AFM test involved setting the tip bias to −10 V, while the sample substrate was connected to ground. Figure 1d illustrates the leakage current distribution associated with the two etching pits obtained through c-AFM testing. The topography and c-AFM images were acquired via two separate scans. The topography scan utilized a laser, while the c-AFM scan excluded any possible photoelectric effects by switching off the laser. Due to the insulating nature of sapphire, the leakage levels observed in this test were relatively lower compared to those on other conductive substrates. The results indicate that the α-type pit corresponding to TED does not introduce significant leakage. On the other hand, the β-type pit, which corresponds to the open-core TSD, exhibits a maximum leakage current of approximately 1.6 pA. The current distribution on the six etching surfaces of the β-type pit is uneven, thus ruling out the possibility that the leakage is caused by a reduction in the Schottky barrier induced by the V-shaped defect on the GaN surface (the six surfaces [10$\bar{1}$0] of the V-shaped pit are equivalent)[47]. Therefore, the increased current at the β-type pit is attributed to the presence of the open-core TSD.

The EFM measurements were conducted to analyze the electric potential distribution of different types of dislocation etching pits. Prior to the EFM scan, the topography was monitored, and the noise in this topography is slightly higher than the previous AFM image due to the influence of the electrostatic force when both the probe tip and sample are biased to +2 V. Figure 1e, f depict the potential distribution images and cutline profile obtained by EFM. To mitigate the impact of the scanning direction on the results, EFM records the scanning results in two directions, with the image scanned first to the right and then to the left. During the scanning process, the β-type pit consistently exhibits a bright area that corresponds to the core of the TSD-induced pits. It can be observed from the light spot at the core and the outer surface that the core potential is approximately 1 V higher than the surface potential. It is important to note that EFM is semi-quantitative, as it involves unmeasurable parameters such as tip capacitances, lock-in amplifier noise and possible charging processes during the scan. As such, the EFM measurement qualitatively confirms that TSD will introduce an electron potential well with a depth of ~1 eV. Based on the above characterization, we can confirm that the screw dislocation has a relatively greater impact on the current leakage and surface potential, which is consistent with the evidence of most studies. It then follows that further research is needed to confirm the dislocation configuration, dislocation-related energy levels, and its trapping mechanism.

Dynamic R_{ON} Testing of HEMTs

After confirming the difference in epitaxial dislocations, we then fabricated 600-V class power HEMTs ($W_G/L_{GS}/L_G/L_{GD}$ = 78,500/3.5/1.8/22 μm) on the two wafers and subjected to hard-switching dynamic R_{ON} testing to verify the effect of dislocations on the dynamic on-resistance of both devices. The test waveform, test platform photo, and test result are depicted in Fig. 2. The device based on the TSD-dominant sample exhibited more pronounced degradation in dynamic R_{ON} compared to the device based on the TED-dominant sample, especially at higher drain bias, while the vertical electric field strength of sapphire substrate GaN devices is more prominent at higher voltages. This discrepancy in dynamic R_{ON} can be attributed to the distinct carrier transport behaviors along the two types of dislocations present in each sample.

TSD-induced level E_{TSD} and TED-induced level E_{TED} via Cryogenic PL

Initially, we employed cryogenic temperature photoluminescence (PL) experiments to identify dislocation-related energy levels and studied the temperature and power dependence to investigate their formation mechanisms. The PL experiment was conducted at a temperature of 2.86 K on both samples using an excitation energy of 5.821 eV which exceeds the bandgap of GaN. The excitation light for the PL measurements was generated through the fourth harmonic generation of a laser beam, with the fundamental frequency light supplied by a mode-locked Ti: Sapphire laser.

Figure 3 illustrates the PL spectra (a) and its near band edge part (b). In the TED-dominant sample, a prominent peak E_{TED} that might correspond to Ga-vacancy TED was observed at an energy level of $E_A = 0.20 \pm 0.02$ eV below the free exciton (FE) energy[44]. In the TSD-dominant samples with GaN NL, a well-identified peak E_{TSD} is observed in the PL spectra within the range of 10-20 meV below the FE peak (approximately 5-15 meV below the donor-bound exciton, DBE). The PL intensity of the peaks in the TSD-dominant samples was baseline-subtracted, and the peak positions were fitted using a Gaussian function, as depicted in Fig. 3c. The fitted peak positions are approximately 3.489 eV for DBE and 3.495 eV for FE. Note that there may be some errors in the fitting of E_{TSD}, and for the analysis of its temperature-dependent and power-dependent PL behavior, 3.483 eV was taken as the peak of E_{TSD}.

The temperature- and power-dependent photoluminescence (PL) measurements of E_{TSD} and E_{TED} were further analyzed to gain insight into their underlying mechanisms. Figure 3d illustrates the correlation between incident laser power intensity and PL intensity at 3.483 eV. The laser power dependence of the PL emission intensity was fitted using the relationship $I \sim P^k$, where I is the photoluminescence intensity, and P is the incident laser power intensity within the power range of 0.1 to 1 μW. The fitting result for I_{TSD} (3.483) ~ P^k yielded $k = 1.4$, indicating a superlinear behavior. This finding strongly suggests that the E_{TSD} peak is associated with non-geminate recombination, likely related to localized shallow bound excitons in the TSD-dominant sample[48–50]. Non-geminate recombination refers to the radiative recombination process involving electrons and holes that originate from separate spatial locations. This superlinear dependence is due to the radiative rate of non-geminate recombination is proportional to the product of the electron density (n_e) and the hole density (n_h) ($R \propto n_e{}^* n_h$), resulting in a superlinear growth of the radiative recombination rate with increasing excitation intensity[51]. Such behavior in GaN has also been attributed to the redirection of electron and hole flow from deep nonradiative centers at low excitation intensity to shallow radiative centers at high excitation intensity[52].

The temperature-dependent PL intensity of E_{TSD} at 3.483 eV is presented in Fig. 3e. An abrupt thermal quenching of PL intensity, I_{TSD}(3.483), was observed at a critical temperature $T_C = 30$ K, with an extracted energy of 14.7 ± 0.4 meV[53]. This value aligns with the energy difference of approximately 12 meV between E_{TSD} (3.483 eV) and FE (3.495 eV), considering the relatively large full width at half maximum (FWHM) of E_{TSD}. This energy difference holds a significant physical interpretation. When the temperature exceeds 30 K, the strongly localized bound excitons surrounding the TSD dislocations undergo dissociation and become thermally activated, transforming into free excitons whose energy level is approximately 14.7 meV higher than the widely observed E_{TSD} in GaN. Consequently, the abrupt thermal

https://doi.org/10.1038/s41467-025-61510-w

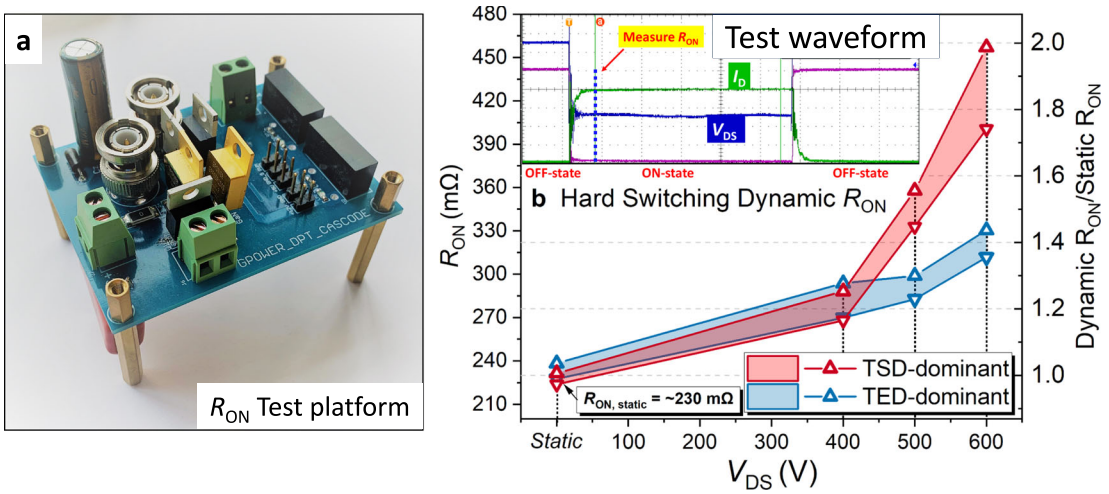

Fig. 2 | Dynamic on-resistance of dislocation-engineered HEMTs. a Photograph of the dynamic R_{ON} test platform. **b** Test waveform and evolution of hard-switching dynamic R_{ON} of HEMTs fabricated on TSD- and TED-dominant samples, respectively.

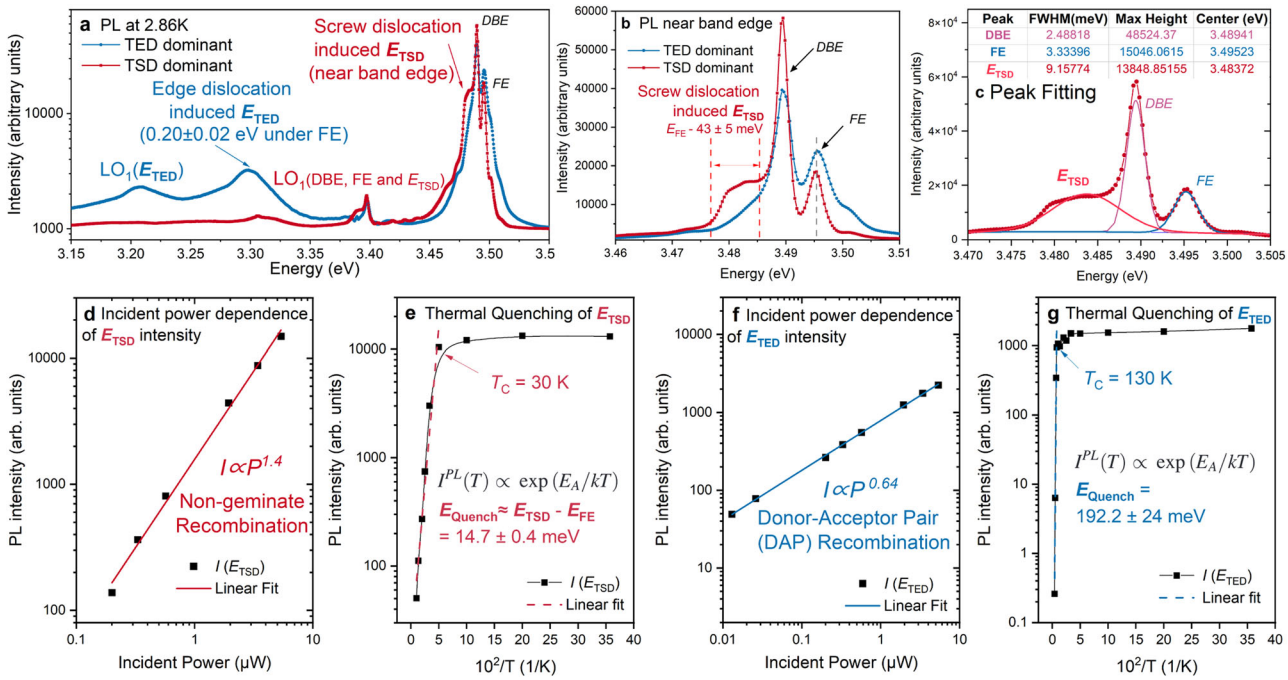

Fig. 3 | PL identification of dislocation-induced states. a PL spectra at 2.86 K, highlighting the near band edge peak E_{TSD} induced by screw dislocations and the peak of E_{TED}, 0.20 ± 0.02 eV below FE, induced by the edge dislocation. E_{TED} is calculated to be related to Ga-vacancy edge dislocations, while E_{TSD} is reported here for the first time. **b** PL spectra near band edge at 2.86 K; **c** Peak fitting result of the PL spectra at band edge for E_{TSD}, FE and DBE. **d** Linear fits of PL intensity of E_{TSD} (3.483 eV) against incident laser power at 2.86 K; (**e**) Temperature dependence of the PL intensity of E_{TSD}. (**f**) Linear fits of PL intensity at E_{TED} (3.30 eV) against incident laser power at 2.86 K; (**g**) Temperature dependence of the PL intensity of E_{TED}, the activation energy of thermal quenching E_{Quench} is derived from the formula in the figure.

quenching observed in the PL spectra occurs. Given that the exciton binding energy in GaN is approximately 28 meV[54], it can be inferred that the open-core TSD induces a localized shallow state, E_{TSD}, with a binding energy range of approximately 38–46 meV.

For E_{TED}, Fig. 3f shows the correlation between the incident laser power intensity and the PL intensity at E_{TED} (3.30 eV). The fitting result for $I_{TED}(3.30) \sim P^k$ yielded $k = 0.64$, indicating a sublinear relationship. This result suggests that the E_{TED} peak arises from donor-acceptor pair (DAP) recombination[55]. As the excitation intensity increases, the donor and acceptor pairs involved in DAP recombination progressively saturate, limiting the capacity of additional excitation to enhance the PL intensity further. The temperature-dependent PL intensity of E_{TED} at 3.30 eV is shown in Fig. 3g. The abrupt thermal quenching of PL intensity $I_{TED}(3.30)$ is observed at a critical temperature $T_C = 130$ K, with an extracted thermal activation energy of 192.2 ± 24 meV[53]. This is consistent with the energy difference of approximately 195 meV between E_{TED} (3.30 eV) and FE (3.495 eV).

Theoretical Analysis of the Open-Core TSDs of GaN

To theoretically understand the newly discovered shallow localized state E_{TSD}, first-principles calculations were performed for the open-core TSD structure using the plane-wave basis Vienna Ab-initio Simulation Package (VASP)[56] with Perdew-Burke-Ernzerhof (PBE) exchange-correlation functional[57] to verify the founded electronic state and

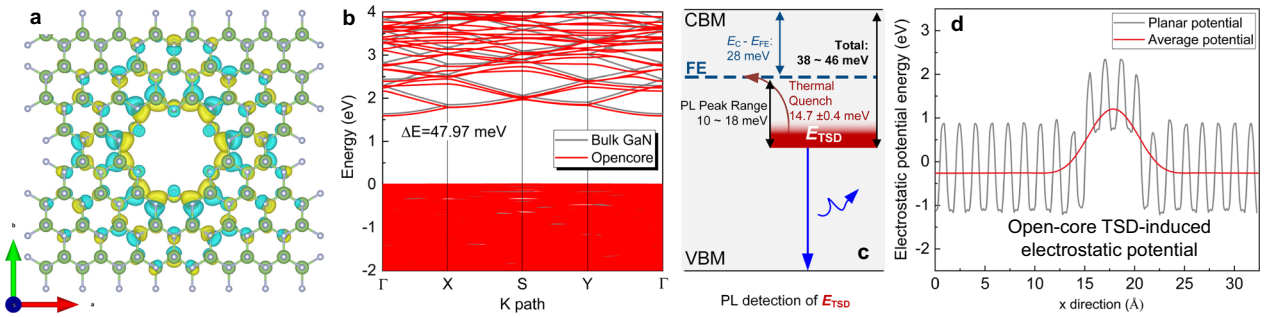

Fig. 4 | Theoretical analysis of the open-core TSDs of GaN. a Schematic plot of the relaxed open-core structure threading screw dislocation of GaN, where the big green and small grey balls represent Ga and N atoms, and the yellow and blue surface represent the isosurface of the differential electronic state distribution in the open-core TSD supercell. The charge isosurface is set to 1e-4 e/Bohr^3. **b** Comparison of the electronic band structures for bulk GaN and open-core type TSD supercell, obtained by PBE functional from first-principles calculation, a shallow energy level at 47.97 meV below the bulk GaN CBM was identified. This calculation result is consistent with the E_{TSD} found in PL (including thermal quenching and level fitting); **c** Summary of TSD induced E_{TSD} detection; **d** Calculation of the electrostatic potential along the core of TSD, the induced potential φ_{TSD} is about 1 eV.

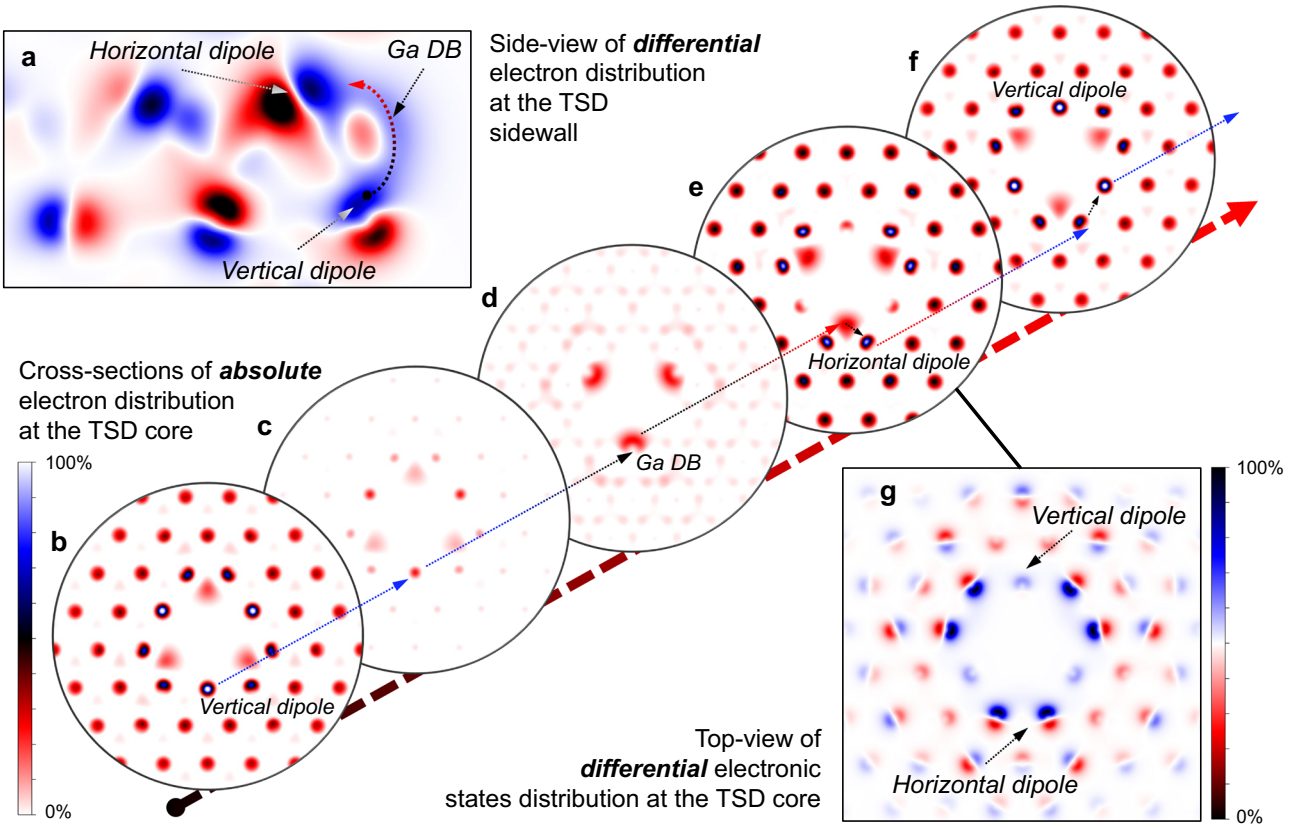

Fig. 5 | Electron-state distribution around open-core TSD in GaN. a Side view of the differential electron state distribution perpendicular to the c-axis. Blue and red sections represent positive and negative differential electronic states, respectively, with electron state density displayed using the K-R-W-B-K palette. **b**–**f** Cross-sectional views of the absolute electron state distribution along the open-core TSD. Demonstrating the roles of Ga dangling bonds and horizontal and vertical Ga-N dipoles in facilitating electron transport along the dislocation sidewall, with electron state density displayed using the W-R-K-B-W palette. **g** Top view of the differential electron state distribution at the position of Fig. 5e, illustrating the dipoles distribute around the dislocation core. The palette used in Fig. 5g is consistent with that in Fig. 5a.

analyze its impact on leakage. The relaxed open-core structure TSD supercell of GaN is depicted in Fig. 4a. The calculated band structures for the GaN host material and the screw dislocation are shown in Fig. 4b. Notably, the screw dislocation (red lines) introduces a shallow donor state at 47.97 meV below the conduction band minimum (CBM) at the zone-center Γ, compared to the host band edges (black lines). This result aligns well with the photoluminescence (PL) measurements. Figure 4c further illustrates the consistency between the experimental detection and theoretical calculation of the E_{TSD} induced by the open-core TSD. The first-principles calculations also demonstrated that the open-core TSDs induce a positive electrostatic potential φ_{TSD} of around +1 eV in Fig. 4d. This finding, combined with the semi-quantitative EFM tests, confirms that TSDs create a potential well in the order of ~1 eV.

The electronic structures of the calculated open-core TSD are presented in Fig. 5, features a series of cross-sectional views

https://doi.org/10.1038/s41467-025-61510-w

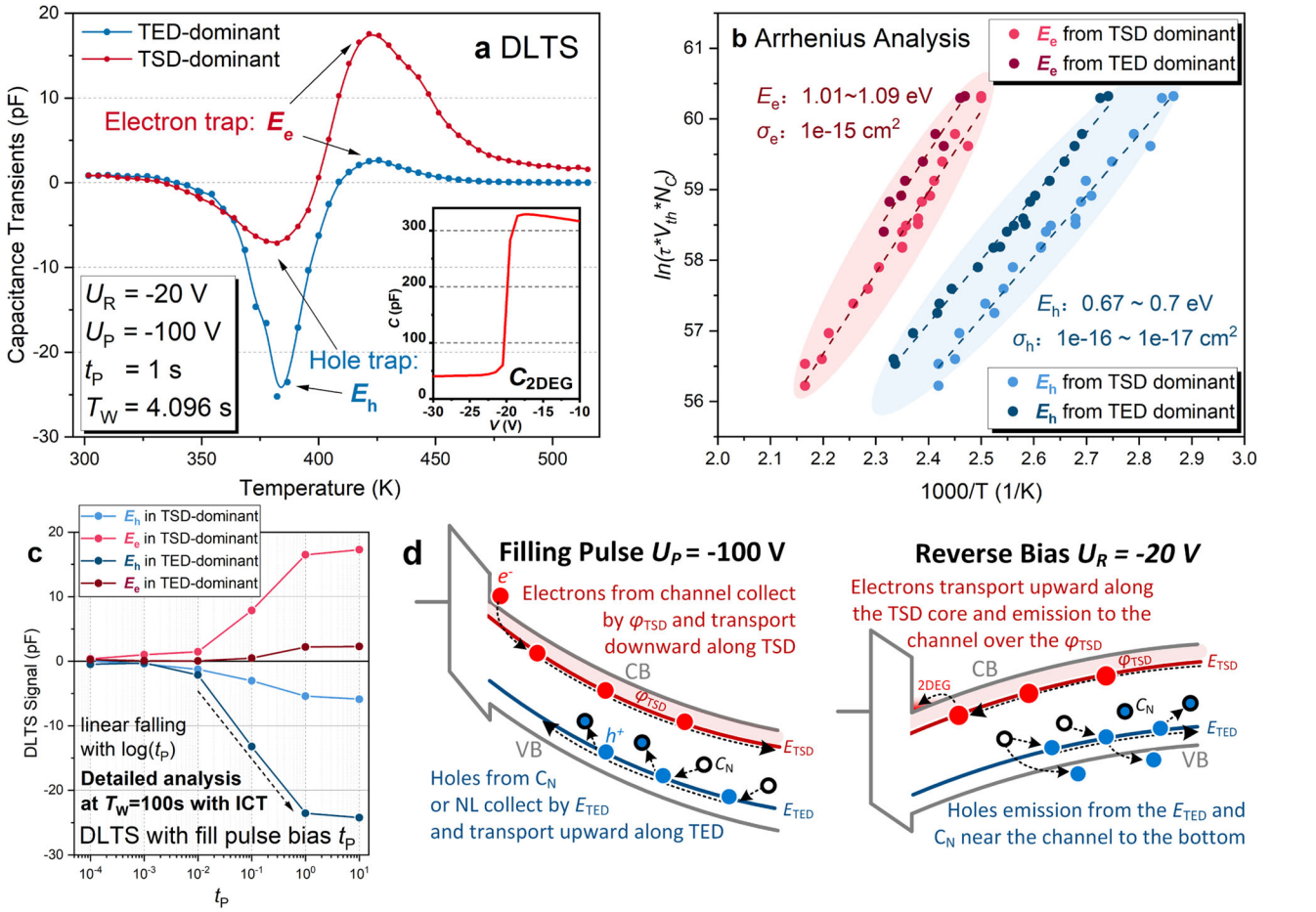

Fig. 6 | DLTS characterization of dislocation-related traps. a DLTS signal of two diodes, remarkable electron trap E_e and hole trap E_h peaks were observed on both diodes. The test conditions are listed in the figure, where U_P is the pulse bias, U_R is the reverse bias which was set to −20V corresponding to C_{2DEG}, t_P is the pulse width and T_W is the duration that the transient is recorded, i.e., the rate window; **b** Arrhenius analysis of E_e and E_h. E_e is widely report as a dislocation related energy level, and it matches well with the density of TSD. **c** Evolution of DLTS signal with t_P. **d** Schematic diagram of the energy band of dislocation assisted trapping and de-trapping of electrons and holes during DLTS measurement.

illustrating both the differential and absolute electronic state distribution along the sidewall of the open-core TSD in GaN. The sequence of cross-sections in Fig. 5b–f corresponds to the position of the curved arrow from vertical dipole via Ga DB to horizontal dipole shown in Fig. 5a. Shear stress induced by the TSD causes distortion of Ga-N bonds along the dislocation sidewall, forming two types of dipoles:

1. Vertical dipoles, with their orientation approximately parallel to the *c*-axis, as inferred from the three vertical shifts of the electronic states near the dislocation cores in Fig. 5e, f as well as the differential electronic state distribution in Fig. 5a. The distortion of vertical Ga-N bonds near the dislocation, as compared to regular Ga-N bonds, leads to the formation of these vertical dipoles.

2. Horizontal dipoles, with their orientation roughly perpendicular to the *c*-axis. These are identified in the differential electron density distribution in Fig. 5a, g, which reveals a ring of dipoles concentrated around the dislocation sidewall, with six horizontal dipole states gathering towards the dislocation core in each GaN bilayer, facilitating electron hopping from Ga DBs to the vertical dipoles.

The differential electron distribution in Fig. 5a highlights two dipoles and Ga DB. These Ga DB and dipoles collectively form a spatially confined charge nanopipe along the dislocation sidewall, facilitating electron transport along the TSD core. The electron conduction pathway through this system involves the following steps:

1. Electron transport via vertical Ga-N dipoles as illustrated in Fig. 5b, c;
2. Electron transfer from vertical Ga-N dipoles to Ga DB as illustrated in Fig. 5c, d;
3. Electron transfer from Ga DB to horizontal Ga-N dipoles, as depicted in Fig. 5e;
4. Transfer from horizontal Ga-N dipoles to vertical Ga-N dipoles, as depicted in Fig. 5f.

This cycle repeats, with the pathway cycling back between the configurations shown in Fig. 5b–f. This intricate sidewall transport pathway significantly reduces the electron hopping distance, promoting efficient electron conduction along the TSD core. Additionally, the spatial separation of electron and hole distribution, with electrons gathering in the core and holes distributed around the core, caused by dipoles near the dislocation core contributes to non-geminate recombination dynamics, as evidenced by the superlinear $I \sim P^k$ relationship of E_{TSD} in PL.

Detection of Dislocation-Related Trap Levels via Deep-Level Transient Spectroscopy

After probing the energy levels by PL, we also need to conduct a detailed study of the dislocation-related non-radiative transition process, because the non-radiative part of dislocations behavior may have

https://doi.org/10.1038/s41467-025-61510-w

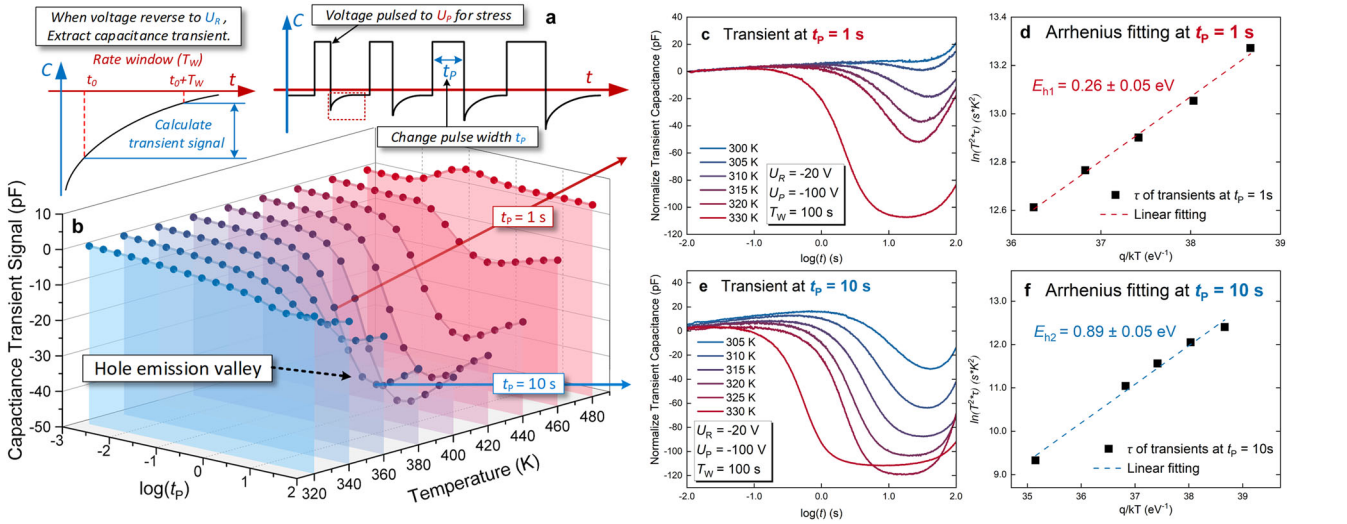

Fig. 7 | ICT reveals TED-assist hole transport. a Test diagram of isothermal capacitance transients (ICT); **b** ICT signal at 300–460 K in TED-dominant with T_W = 100 s, the hole emission signal falling logarithmically with t_P and saturate. To eliminate the interference of the electron emission, transients at 305–330 K were taken for analysis in Fig. 5c–f. Transient Fitting: (**c**, **d**) At t_P = 1 s, hole traps begin to emit. The activation energy extracted from the transient at t_P = 1 s is E_{h1} = 0.26 ± 0.01 eV; (**e**, **f**) At t_P = 10 s, hole traps signal saturated, the activation energy extracted is E_{h2} = 0.89 ± 0.05 eV.

a more direct relationship with the electrical properties of the GaN power device. Deep-level transient spectroscopy (DLTS) was employed to obtain the trapping behavior associated with TEDs and TSDs. Two SiN_x/AlGaN/GaN MIS diodes with TSD- and TED-dominant epilayers were fabricated for the dislocation-related levels detection. The DLTS setup was referred to 1-MHz C-V characteristics. In Fig. 6a, both electron trap E_e and hole trap E_h have been detected in both TSD- and TED-dominant devices. Arrhenius analysis of tahe two peaks is shown in Fig. 6b. On the one hand, E_e has been reported to be related to dislocations[58]. The energy level depth and capture cross section of E_e are consistent with the calculated φ_{TSD} in Fig. 4d. The FWMH of φ_{TSD} is about 0.5 nm, its induced potential well area is ~10^{-15} cm^{-2}, and the level is about ~1 eV below the CBM. The potential well may be introduced by strain near the dislocation core. On the other hand, the signals of the hole traps exhibit a logarithmic dependence on the filling pulse width t_P in Fig. 6c, indicating the presence of line defects such as dislocations. The hole traps E_h = 0.67 ~ 0.7 eV have been reported to be related to the emission of C_N in carbon-doped buffer through the defect band above valence band maximum (VBM), which may be introduced by edge dislocations[59]. Figure 6d briefly depicts the capture and emission process of the traps in the DLTS test.

It is worth noting that since the sources of holes in GaN devices are very limited, in general power devices (except gate injection transistor structure), in addition to collision ionization, the other main source is the ionized hole in the carbon-doped GaN (GaN:C) buffer. The holes generated by high-field collision ionization are mainly concentrated on the AlGaN/GaN channel and collected by the electrode on the top. The whole process is not strongly related to the vertical transport via dislocations. The hole transport process of dislocations is closely related to carbon doping-induced hole traps. Therefore, the hole transport mechanism through dislocations needs to be studied synchronously together with the interplay of dislocations and traps in C-doped GaN buffers.

TED-assisted hole trapping/de-trapping dynamics confirmed by ICT

The interaction between the hole potential well induced by TED[60] and the C-related hole trap in buffer was investigated by isothermal capacitance transients (ICT) test to conduct a detailed analysis for the DLTS detected level E_h that may involve both dislocations and carbon doping. Figure 7a, b demonstrate the test diagram and result with a monitored rate window (T_W) of 100 s of ICT in TED-dominant device. The hole emission signal exhibits a falling edge (at t_P = 0.1 to 10 s) followed by saturation (at $t_P \geq 10$ s). By extracting the emission time constants (τ_e) and performing the Arrhenius fitting at each stage, we obtain E_{h1} = 0.26 ± 0.05 eV for the falling process at t_P = 1 s, and E_{h2} = 0.89 ± 0.05 eV for the saturation process at t_P = 10 s. Combined with the activation energy E_h measured by DLTS, this 3-segment hole emission phenomenon that is related to the interaction between TED-induced level and C_N can be pulled out in the next section.

The hole trapping and de-trapping dynamics detected by DLTS and ICT can be categorized into three distinct stages, as summarized in Fig. 8:

(1) Fast emission: Detected through DLTS using a short rate window (T_W = 4.096 s), this phase involves a reduction in vertical resistivity near TEDs, promoting the rapid ionization of holes trapped in C_N and their subsequent emission into TED-induced energy levels (E_{TED}). The activation energy for this stage is approximately $E_h = E(C_N)$-E_{TED} = 0.67 ~ 0.7 eV, with a short τ_e (<4 s).

(2) Slow emission: Revealed by ICT under a large rate window (T_W = 100 s), this phase occurs when holes trapped within TEDs undergo vertical hopping before emission. Despite having a longer τ_e, the activation energy for this stage ($E_{h1} \approx E(C_N)$-$E_h \approx E_{TED}$) is lower (0.26 ± 0.05 eV above the VBM). The discrepancy arises from differences in temperature and excitation conditions: DLTS measures ionization energy, while PL captures radiative recombination, often reduced by multi-phonon emission[61].

(3) Direct emission: Also observed under ICT with a large rate window, this phase dominates once TEDs are fully occupied, leading to the direct emission of holes from C_N traps into the VBM. The activation energy for this phase corresponds to $E_{h2} = E(C_N)$ = 0.89 ± 0.05 eV. During this process, photon emission only occurs due to donor-acceptor pair (DAP) transitions between the GaN donor state and E_{TED}. The real-space transfer of holes between C_N sites and TED cores involves nonradiative transitions, detectable only through electrical measurements such as DLTS and ICT.

For TSD-induced electron trapping as also shown in Fig. 8, electrons are first trapped by the electron potential well φ_{TSD} of about 1 eV

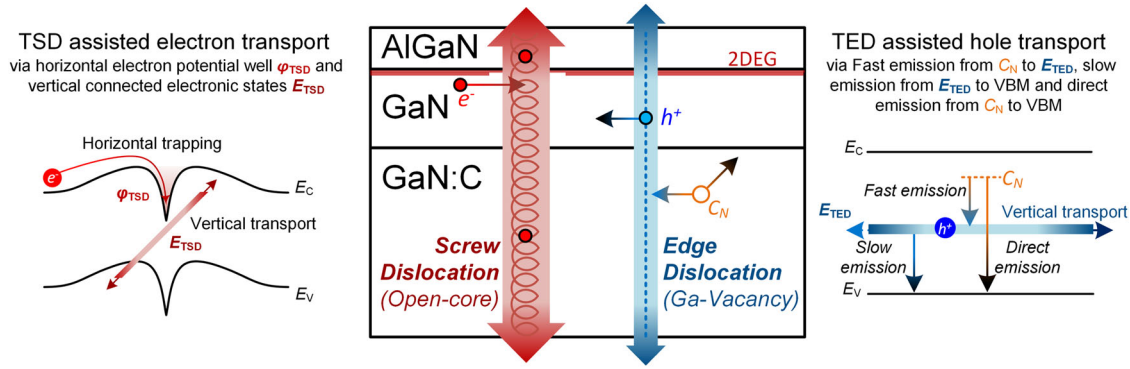

Fig. 8 | Dual-path electron–hole transport model. Schematic diagram of TSD-assisted electron transport via E_{TSD} and φ_{TSD}, and TED-assisted hole transport between E_{TED} and C_N through Fast emission, Slow emission and Direct emission.

introduced by TSD on the *c*-plane; after falling into the TSD core, electrons can further be transported vertically by the shallow energy level localized state E_{TSD}. In this process, PL can detect the emission process of the shallow localized shallow bound excitation of E_{TSD}, while the electron horizontal transport and trapping process of non-radiative recombination does not emit photons and can only be detected by DLTS and EFM.

Discussion

The mechanisms underlying charge carrier transport mediated by threading screw dislocations (TSDs) and threading edge dislocations (TEDs) in GaN epitaxial layers offer a nuanced perspective on the interplay between dislocations and dopant-induced traps. By analyzing their distinct contributions, this study highlights how dislocations act as both facilitators and impediments to device performance, with implications for optimizing GaN epitaxy and device engineering.

TSD-Induced Electron Transport and Trapping

TSDs serve as vertical pathways for electron transport through the formation of shallow energy levels (E_{TSD}) and horizontal electron trapping via deep potential wells (φ_{TSD}). The ~1 eV potential wells result from structural distortions along the dislocation core, attributed to Ga–N dipoles, as corroborated by first-principles calculations. The calculations demonstrate that the open-core TSDs induce Ga-N dipoles and Ga dangling bonds along the dislocation sidewalls, introducing electronic states that are longitudinal connected and ultimately forming vertical conducting paths. An open-core screw dislocation density of $10^8\,cm^{-2}$ introduces electron traps with a concentration of approximately $1.1\times10^{16}\,cm^{-3}$ (Table 1), attributed to the presence of three Ga DBs in each Ga-N diatomic layer in each open-core screw dislocation unit cell. TSD induces shallow localized states (E_{TSD}) with binding energies of 38–46 meV below the conduction band minimum enable vertical transport along the TSD core, as evidenced by photoluminescence (PL) measurements. The c-AFM provides direct evidence that open-core TSD introduces a longitudinal leakage path. As a result, TSDs exacerbate electron leakage, particularly under high electric fields, leading to increased current collapse and dynamic resistance (R_{ON}) degradation.

TED-Assisted Hole Transport and Redistribution

In contrast, TEDs primarily facilitate hole transport by introducing trap levels (E_{TED}) above the VBM, which interact with carbon-related (C_N) traps in the GaN buffer. The ICT and DLTS measurements identify a three-phase hole emission process involving fast, slow, and direct emission stages. Initially, TEDs reduce local resistivity, enabling rapid ionization of holes from C_N traps into E_{TED} (activation energy ~0.7 eV). Subsequently, slow emission involves vertical hopping of holes with a lower activation energy (~0.26 eV), before transitioning to direct emission from C_N traps into the valence band maximum (~0.89 eV).

The defect concentration associated with Ga-vacancy type edge dislocations is based on electronic structure calculations provided in reference[44]. Specifically, each Ga-vacancy edge dislocation introduces one Ga vacancy in every Ga-N bilayer (each edge dislocation unit cell contains one Ga vacancy), where the *p*-orbitals of the nitrogen atoms located above and below the missing Ga atom create a hole trap, positioned approximately 0.2 eV above the VBM. Thus, an edge dislocation density of $10^8\,cm^{-2}$ introduces a continuous distribution of hole traps with a concentration of $\sim1.9\times10^{15}\,cm^{-3}$ in the GaN bulk. This linear extended hole trap introduced by TED plays a compensatory role by redistributing trapped electrons in buffer and mitigating TSD-induced leakage effects. Highlights the importance of TEDs in maintaining dynamic resistance stability in GaN-based devices.

Interplay Between TSDs and TEDs in Device Performance

In the device, during hard-switching operations, TSD cause electron trapping to the C-doped layer, resulting in the depletion of the 2DEG and a degradation of the dynamic R_{ON}. While TED facilitates the redistribution of holes in the C-doped GaN layer and the release of trapped electrons near the channel, thereby aiding in suppressing the degradation of dynamic R_{ON}. The dynamic performance variations between devices can be attributed to differing the ratios of TSDs and TEDs. Table 1 provide a summary of the estimated dislocation-induced trap densities between the two samples in this study. The TSD-dominant device exhibited an electron trap density introduced by TSDs of $\sim5\times10^{16}\,cm^{-3}$, with TED-induced hole trap concentration of $\sim0.72\times10^{16}\,cm^{-3}$. The rapid vertical filling of buffer defects by electrons could not be effectively balanced by the lower concentration of hole transport channels introduced by TEDs. In contrast, for the TED-dominant device, the TSD-induced electron trap concentration was approximately $0.2\times10^{16}\,cm^{-3}$, while the TED-induced hole trap density was significantly higher, around $3.4\times10^{16}\,cm^{-3}$. Although the source of holes is limited and the sidewall dipoles introduced by TSDs may promote easier vertical electron transport, the more abundant hole transport pathways effectively compensate for these effects. This analysis is further corroborated by dynamic R_{ON} measurements in Fig. 2, where the TED-dominant devices showed a linear increase in R_{ON} degradation with rising V_{DS} at higher voltages, continuing the trend observed at lower voltages. This degradation may be related to interface states and other bulk defects in GaN. In contrast, TSD-dominant devices exhibited a pronounced increase in dynamic R_{ON} at higher voltages, driven by the intensified vertical electric field. This analysis reflects the current state of research, where conventional epitaxial growth, typically with an AlN nucleation layer, is TED-dominant. Despite the high dislocation densities in GaN, the mutual

compensation between TSDs and TEDs enables the continued functionality of modern GaN devices.

Broader Implications and Future Research

The findings of this study offer a framework for defect engineering in GaN epitaxial layers, emphasizing the need to tailor dislocation densities to balance electron and hole transport pathways and leakage channels. TSDs, despite their drawbacks, provide essential electron vertical transport channels, while TEDs mitigate leakage effects by facilitating efficient hole redistribution.

Future research should focus on the dynamic behavior of threading mixed dislocations and their potential synergistic effects on carrier transport. Furthermore, investigating dislocation interactions under operational conditions, such as high electric fields and thermal stress, may further elucidate their role in device performance and reliability.

Moreover, extending the understanding of dislocation-mediated transport to other materials beyond GaN, including semiconductors such as Si, SiC, and diamond, as well as oxides like ZnO and perovskites, could expand the scope of dislocation-engineering strategies. These materials, with their distinct electronic structures and defect physics, may offer complementary insights into the role of dislocations. Such advancements could lead to the development of novel dislocation-engineered devices and breakthroughs in one-dimensional electronic systems, paving the way for innovative applications in power electronics, high-frequency devices, and next-generation logic devices.

Methods

GaN device epitaxial

The GaN device epitaxial structure was grown under nitrogen-rich conditions by MOCVD on sapphire substrates, starting with a low-temperature GaN or AlN nucleation layer to promote smooth epitaxial growth. A 3D-GaN transitional layer was then deposited to control dislocations, followed by a carbon-doped GaN bulk layer to enhance its breakdown performance. A GaN channel layer was subsequently grown to optimize electron transport. An AlN spacer was introduced to separate the GaN channel from the AlGaN barrier layer, which induces a two-dimensional electron gas (2DEG) at the interface, essential for high electron mobility. A SiN_x passivation layer was used to suppress surface states at the AlGaN surface. This epitaxial design is well-suited for high-performance GaN-based devices, particularly for high-power applications.

Characterization and Measurements

The atomic force microscopy (AFM), electrostatic force microscopy (EFM), and conductive-AFM (c-AFM) images were obtained using a Park XE-70 system. Photoluminescence (PL) experiments were conducted at a temperature of 2.86 K on both samples using an excitation energy of 5.821 eV, which exceeds the bandgap of GaN. The excitation light for the PL measurements was generated by the fourth harmonic generation of a laser beam, with the fundamental frequency provided by a mode-locked Ti laser source from Coherent Chameleon Ultra II. The imaging spectrometer used for the PL experiment was the HORIBA iHR550. Deep-level transient spectroscopy (DLTS) measurements were carried out using the Phystech FT-1230 HERA system. During the buffer traps emission/measurement phase, the sample was biased at $U_R = -20$ V, near the threshold of two-dimensional electron gas depletion, with a pulse to $U_P = -100$ V for $t_P = 1$ s to fill dislocation-related traps. A double boxcar approach was used to record thermally assisted trap emission transients from 12 ms after the pulse, with a rate window T_W of 4.096 s. To capture the evolution of E_e with pulse time (t_P) in detail, a longer T_W of 100 s was employed. To eliminate E_h emission, the high-temperature side ($T = 450$ K) signal was used to study the capture behavior of E_e. Detailed analytical methods are referenced in the literature[62].

First-principles calculation

The first-principles calculation for the open-core type TSD structure was performed using the plane-wave basis code Vienna ab-initio simulation package (VASP)[56] with Perdew–Burke–Ernzerhof (PBE) exchange correlation functional[57]. The pseudopotential is described by the projector-augmented-wave (PAW) method[63] with a cutoff energy of 500 eV. For structure relaxations, the energy convergence is set to be 10^{-5} eV, while the force on each atom is converged to less than 0.02 eV/Å. Ga 3 *d* electrons are also included in the valence electrons. We created a dislocation structure based on a $10 \times 5 \times 1$ GaN supercell[3]. It is found that the open-core screw dislocation with a Burgers vector of 1c is energetically stable, exhibiting a diameter of 7.45 Å, in good agreement with the previous work[38]. The relaxed open-core structure containing up to 388 atoms. Note that no additional Heyd-Scuseria-Ernzerhof (HSE) functional calculation is used in this work, due to the limit of the computing resources. The electrostatic potential, electronic band structures, and carrier concentration distribution around the screw dislocation core are extracted from this calculation.

Data availability

All data that support the findings of this study can be found within this article and its supplementary information. The source data, backing the findings of this study, are provided with this paper. Any correspondence and material requests should be addressed to S. Huang. Source data are provided with this paper.

Code availability

No custom code was generated or used in this study.

References

1. Amodeo, R. J. & Ghoniem, N. M. Dislocation dynamics. II. Applications to the formation of persistent slip bands, planar arrays, and dislocation cells. *Phys. Rev. B* **41**, 6968–6976 (1990).
2. Amodeo, R. J. & Ghoniem, N. M. Dislocation dynamics. I. A proposed methodology for deformation micromechanics. *Phys. Rev. B* **41**, 6958–6967 (1990).
3. Béré, A. & Serra, A. Atomic structure of dislocation cores in GaN. *Phys. Rev. B* **65**, 205323 (2002).
4. Sun, B. et al. Dislocation-induced thermal transport anisotropy in single-crystal group-III nitride films. *Nat. Mater.* **18**, 136–140 (2019).
5. Arakawa, K. et al. Observation of the one-dimensional diffusion of nanometer-sized dislocation loops. *Science* **318**, 956–959 (2007).
6. Jena, D. Spin scattering by dislocations in III-V semiconductors. *Phys. Rev. B* **70**, 245203 (2004).
7. Reiche, M. et al. Electronic properties of dislocations. *Appl. Phys. A* **122**, 389 (2016).
8. Jin, Z., Li, X., Mullen, J. T. & Kim, K. W. Intrinsic transport properties of electrons and holes in monolayer transition-metal dichalcogenides. *Phys. Rev. B* **90**, 045422 (2014).
9. Kittler, M. et al. Transport of charge carriers along dislocations in Si and Ge. *Phys. Status Solidi A* **216**, 1900287 (2019).
10. Armstrong, M. D., Lan, K.-W., Guo, Y. & Perry, N. H. Dislocation-mediated conductivity in oxides: progress, challenges, and opportunities. *ACS Nano* **15**, 9211–9221 (2021).
11. Reiche, M. et al. On the electronic properties of a single dislocation. *J. Appl. Phys.* **115**, 194303 (2014).
12. Reiche, M., Kittler, M., Krause, M. & Übensee, H. Electrons on dislocations. *Phys. Status Solidi C* **10**, 40–43 (2013).
13. Reiche, M., Kittler, M., Uebensee, H., Pippel, E. & Hopfe, S. Dislocations as native nanostructures - electronic properties. *Adv. Nano Res.* **2**, 1–14 (2014).

14. Koller, C., Pobegen, G., Ostermaier, C., Huber, M. & Pogany, D. The interplay of blocking properties with charge and potential redistribution in thin carbon-doped GaN on n-doped GaN layers. *Appl. Phys. Lett.* **111**, 032106 (2017).
15. Reiche, M. et al. Dislocation-Based Si-Nanodevices. *Jpn. J. Appl. Phys.* **49**, 04DJ02 (2010).
16. Reiche, M., Kittler, M., Scholz, R., Hähnel, A. & Arguirov, T. Structure and properties of dislocations in interfaces of bonded silicon wafers. *J. Phys.: Conf. Ser.* **281**, 012017 (2011).
17. Schreck, M. et al. Charge carrier trapping by dislocations in single crystal diamond. *J. Appl. Phys.* **127**, 125102 (2020).
18. De Souza, R. A. Transport properties of dislocations in SrTiO3 and other perovskites. *Curr. Opin. Solid State Mater. Sci.* **25**, 100923 (2021).
19. Kohary, K. et al. One-dimensional hopping transport in disordered organic solids. II. Monte Carlo simulations. *Phys. Rev. B* **63**, 094202 (2001).
20. Tito, M. A. & Pusep, Y.uA. Localized-to-extended-states transition below the Fermi level. *Phys. Rev. B* **97**, 184203 (2018).
21. Bougrioua, Z., Farvacque, J. L. & Ferré, D. Effects of dislocations on transport properties of two dimensional electron gas. I. Transport at zero magnetic field. *J. Appl. Phys.* **79**, 1536–1545 (1996).
22. Hashimoto, T., Wu, F., Speck, J. S. & Nakamura, S. A GaN bulk crystal with improved structural quality grown by the ammonothermal method. *Nat. Mater.* **6**, 568–571 (2007).
23. Wu, X. H. et al. Dislocation generation in GaN heteroepitaxy. *J. Cryst. Growth* **189–190**, 231–243 (1998).
24. Lester, S. D., Ponce, F. A., Craford, M. G. & Steigerwald, D. A. High dislocation densities in high efficiency GaN-based light-emitting diodes. *Appl. Phys. Lett.* **66**, 1249–1251 (1995).
25. Hamachi, T. et al. Comprehensive analysis of current leakage at individual screw and mixed threading dislocations in freestanding GaN substrates. *Sci. Rep.* **13**, 2436 (2023).
26. Rackauskas, B., Dalcanale, S., Uren, M. J., Kachi, T. & Kuball, M. Leakage mechanisms in GaN-on-GaN vertical pn diodes. *Appl. Phys. Lett.* **112**, 233501 (2018).
27. Wohlfahrt, M., Uren, M. J., Yin, Y., Lee, K. B. & Kuball, M. Vertical field inhomogeneity associated with threading dislocations in GaN high electron mobility transistor epitaxial stacks. *Appl. Phys. Lett.* **119**, 243502 (2021).
28. Uren, M. J. et al. Leaky Dielectric' Model for the Suppression of Dynamic $R_\mathrmON$ in Carbon-Doped AlGaN/GaN HEMTs,. *IEEE Trans. Electron Devices* **64**, 2826–2834 (2017).
29. Besendörfer, S. et al. Interplay between C-doping, threading dislocations, breakdown, and leakage in GaN on Si HEMT structures. *AIP Adv.* **10**, 045028 (2020).
30. Hinoki, A. et al. Effects of traps formed by threading dislocations on off-state breakdown characteristics in GaN buffer layer in AlGaN/GaN Heterostructure Field-Effect Transistors. *Appl. Phys. Express* **1**, 011103 (2008).
31. Usami, S. et al. Correlation between dislocations and leakage current of p-n diodes on a free-standing GaN substrate. *Appl. Phys. Lett.* **112**, 182106 (2018).
32. Wang, J. et al. Do all screw dislocations cause leakage in GaN-based devices?. *Appl Phys. Lett.* **116**, 062104 (2020).
33. Shiojima, K., Suemitsu, T. & Ogura, M. Correlation between current–voltage characteristics and dislocations for *n* -GaN Schottky contacts. *Appl. Phys. Lett.* **78**, 3636–3638 (2001).
34. Usami, S. et al. Correlation between nanopipes formed from screw dislocations during homoepitaxial growth by metal-organic vapor-phase epitaxy and reverse leakage current in vertical p–n diodes on a free-standing GaN substrates. *Jpn. J. Appl. Phys.* **58**, SCCB24 (2019).
35. Lee, S. W. et al. Origin of forward leakage current in GaN-based light-emitting devices. *Appl. Phys. Lett.* **89**, 132117 (2006).
36. Kim, B. et al. Investigation of leakage current paths in n-GaN by conductive atomic force microscopy. *Appl. Phys. Lett.* **104**, 102101 (2014).
37. Gröger, R., Leconte, L. & Ostapovets, A. Structure and stability of threading edge and screw dislocations in bulk GaN. *Comput. Mater. Sci.* **99**, 195–202 (2015).
38. Elsner, J. et al. Theory of threading edge and screw dislocations in GaN. *Phys. Rev. Lett.* **79**, 3672–3675 (1997).
39. Northrup, J. E. Screw dislocations in GaN: the Ga-filled core model. *Appl. Phys. Lett.* **78**, 2288–2290 (2001).
40. Vennéguès, P., Beaumont, B., Vaille, M. & Gibart, P. Study of open-core dislocations in GaN films on (0001) sapphire. *Appl. Phys. Lett.* **70**, 2434–2436 (1997).
41. Lymperakis, L., Neugebauer, J., Albrecht, M., Remmele, T. & Strunk, H. P. Strain induced deep electronic states around threading dislocations in GaN. *Phys. Rev. Lett.* **93**, 196401 (2004).
42. Wright, A. F. & Grossner, U. The effect of doping and growth stoichiometry on the core structure of a threading edge dislocation in GaN. *Appl. Phys. Lett.* **73**, 2751–2753 (1998).
43. Leung, K., Wright, A. F. & Stechel, E. B. Charge accumulation at a threading edge dislocation in gallium nitride. *Appl. Phys. Lett.* **74**, 2495–2497 (1999).
44. Lee, S. M. et al. Electronic structures of GaN edge dislocations. *Phys. Rev. B* **61**, 16033–16039 (2000).
45. Hong, S. K., Yao, T., Kim, B. J., Yoon, S. Y. & Kim, T. I. Origin of hexagonal-shaped etch pits formed in (0001) GaN films. *Appl. Phys. Lett.* **77**, 82–84 (2000).
46. Lu, L. et al. Microstructure and origin of dislocation etch pits in GaN epilayers grown by metal organic chemical vapor deposition. *J. Appl. Phys.* **104**, 123525 (2008).
47. Shiojiri, M., Chuo, C. C., Hsu, J. T., Yang, J. R. & Saijo, H. Structure and formation mechanism of V defects in multiple InGaN/GaN quantum well layers. *J. Appl. Phys.* **99**, 073505 (2006).
48. Taguchi, T., Shirafuji, J. & Inuishi, Y. Excitonic emission in cadmium telluride. *Phys. Status Solidi B* **68**, 727–738 (1975).
49. Ikhmayies, S. J. & Ahmad-Bitar, R. N. Dependence of the photoluminescence of CdS:In thin films on the excitation power of the laser. *J. Lumin.* **149**, 240–244 (2014).
50. Fang, R. C. Emission properties of amorphous silicon and carbon films. *J. Lumin.* **48–49**, IN5–IN635 (1991).
51. Proctor, C. M., Kuik, M. & Nguyen, T.-Q. Charge carrier recombination in organic solar cells. *Prog. Polym. Sci.* **38**, 1941–1960 (2013).
52. Reshchikov, M. A., Olsen, A. J., Bishop, M. F. & McMullen, T. Superlinear increase of photoluminescence with excitation intensity in Zn-doped GaN. *Phys. Rev. B* **88**, 075204 (2013).
53. Reshchikov, M. A. Mechanisms of thermal quenching of defect-related luminescence in semiconductors. *Phys. Status Solidi A* **218**, 2000101 (2021).
54. Reshchikov, M. A. Measurement and analysis of photoluminescence in GaN. *J. Appl. Phys.* **129**, 121101 (2021).
55. Tarekegne, A. T., Shi, X., Gan, Y., Chen, Y. & Ou, H. Dependence of photoluminescence emission on excitation power and temperature in highly doped 6H- Si C. *Phys. Rev. Appl.* **13**, 064002 (2020).
56. Kresse, G. & Furthmüller, J. Efficient iterative schemes for ab initio total-energy calculations using a plane-wave basis set. Phys. Rev. B **54**, 11169, Accessed: Apr. 25, 2024. [Online]. Available: https://doi.org/10.1103/PhysRevB.54.11169, (1996).
57. Perdew, J. P., Burke, K. & Ernzerhof, M. Generalized gradient approximation made simple. *Phys. Rev. Lett.* **77**, 3865–3868 (1996).
58. Fang, Z. Q., Look, D. C. & Polenta, L. Dislocation-related electron capture behaviour of traps in n-type GaN. *J. Phys. Condens. Matter* **14**, 13061–13068 (2002).
59. Koller, C., Pobegen, G., Ostermaier, C. & Pogany, D. Evidence of defect band in carbon-doped GaN controlling leakage current and trapping dynamics, in *2017 IEEE International Electron Devices*

Meeting (IEDM), San Francisco, CA, USA: IEEE, Dec, 33.4.1-33.4.4. https://doi.org/10.1109/IEDM.2017.8268491, (2017).
60. Cherns, D. & Jiao, C. G. Electron holography studies of the charge on dislocations in GaN. *Phys. Rev. Lett.* **87**, 205504 (2001).
61. Fregolent, M. et al. Advanced defect spectroscopy in wide-bandgap semiconductors: review and recent results. *J. Phys. D: Appl. Phys.* **57**, 433002 (2024).
62. Huang, S. et al. Capture and emission mechanisms of defect states at interface between nitride semiconductor and gate oxides in GaN-based metal-oxide-semiconductor power transistors. *J. Appl. Phys.* **126**, 164505 (2019).
63. Blöchl, P. E. Projector augmented-wave method. *Phys. Rev. B* **50**, 17953–17979 (1994).

Acknowledgements

This work was supported by the National Natural Science Foundation of China (Grant 62334012, S.H.; Grant 62304252, Y.Y.), the CAS-Croucher Funding Scheme (Grant CAS22801, S.H.) and the Joint Laboratory of Microelectronics (Grant JLFS/E-601/24, S.H.).

Author contributions

Y.Y. conceived and designed the study, performed most of the experiments, carried out mechanism analysis, prepared the figures and drafted the manuscript; S.H. supervised the project, provided technical guidance, contributed to the mechanism discussions, revised the manuscript, and secured the funding; R.C. performed first-principles calculations and assisted in mechanism interpretation, with additional modelling contributed by Z.Z.; X.W. and Q.J. coordinated the project and supplied resources; J.S. conducted the AFM, EFM and C-AFM measurements; C.Z. performed the DLTS and ICT experiments; J.L. carried out epitaxial characterization; K.W. and F.G. executed the dislocation etch-pit experiments; X.L. provided resource support and technical guidance; Y.P. offered process support for device fabrication; H.Z. assisted in epitaxial growth; H.Q. measured the dynamic on-resistance; G.L. and N.T. acquired the PL measurement and contributed to their interpretation; J.-W.L. and W.G. verified the mechanism analysis and provided technical guidance; B.S. and K.J.C. supervised the research and provided overall technical guidance. All authors participated in the writing and approved the final version of the manuscript.

Competing interests

The authors declare no competing interests.

Additional information

Supplementary information The online version contains supplementary material available at https://doi.org/10.1038/s41467-025-61510-w.

Correspondence and requests for materials should be addressed to Sen Huang, Xinyu Liu, Bo Shen or Kevin J. Chen.

Peer review information *Nature Communications* thanks Moonsang Lee, and the other, anonymous, reviewer(s) for their contribution to the peer review of this work. A peer review file is available.

Reprints and permissions information is available at http://www.nature.com/reprints

Publisher's note Springer Nature remains neutral with regard to jurisdictional claims in published maps and institutional affiliations.

Open Access This article is licensed under a Creative Commons Attribution-NonCommercial-NoDerivatives 4.0 International License, which permits any non-commercial use, sharing, distribution and reproduction in any medium or format, as long as you give appropriate credit to the original author(s) and the source, provide a link to the Creative Commons licence, and indicate if you modified the licensed material. You do not have permission under this licence to share adapted material derived from this article or parts of it. The images or other third party material in this article are included in the article's Creative Commons licence, unless indicated otherwise in a credit line to the material. If material is not included in the article's Creative Commons licence and your intended use is not permitted by statutory regulation or exceeds the permitted use, you will need to obtain permission directly from the copyright holder. To view a copy of this licence, visit http://creativecommons.org/licenses/by-nc-nd/4.0/.

© The Author(s) 2025